MIT Open Access Articles

Complex Oxides under Simulated Electric Field: Determinants of Defect Polarization in AB O 3 Perovskites

Complex Oxides under Simulated Electric Field: Determinants of Defect Polarization in *ABO*₃ Perovskites

Yen-Ting Chi, Krystyn J. Van Vliet,* Mostafa Youssef,* and Bilge Yildiz*

Polarization of ionic and electronic defects in response to high electric fields plays an essential role in determining properties of materials in applications such as memristive devices. However, isolating the polarization response of individual defects has been challenging for both models and measurements. Here the authors quantify the nonlinear dielectric response of neutral oxygen vacancies, comprised of strongly localized electrons at an oxygen vacancy site, in perovskite oxides of the form *ABO*₃. Their approach implements a computationally efficient local Hubbard *U* correction in density functional theory simulations. These calculations indicate that the electric dipole moment of this defect is correlated positively with the lattice volume, which they varied by elastic strain and by A-site cation species. In addition, the dipole of the neutral oxygen vacancy under electric field increases with increasing reducibility of the B-site cation. The predicted relationship among point defect polarization, mechanical strain, and transition metal chemistry provides insights for the properties of memristive materials and devices under high electric fields.

1. Introduction

Point defects such as oxygen vacancies play an important role in memristive devices.[1–4] Particularly in devices comprising thin films, these materials operate under high electric fields (on the order of megavolt per centimeter). Recent studies have shown

that polarization of point defects under such high electric fields can strongly impact defect formation,[5] transport,[6] and distribution, as well as dielectric response,[7] which are integral to device performance. In memristive devices, the formation and migration of oxygen vacancies under strong electric fields directly facilitate conductive filament growth,[8,9] which in turn governs device switching speed, state stability, and durability.[1,8] While earlier works have demonstrated the significance of defect polarization to device performance under high external electric field, it is important to further identify and quantify the impact of factors controlling field-dependent polarization of point defects, and this knowledge can facilitate materials design for devices with targeted functionalities.[8,10]

However, decoupling the factors driving defect polarization in functional oxides has been non-trivial. Using state-of-the-art aberration-corrected scanning transmission electron microscopy (AC-STEM), Gao et al.[11] demonstrated direct imaging of local charge density in a SrTiO₃-BiFeO₃ heterojunction with sub-Angstrom resolution. Kumar et al.[12] have also shown nanoscale polarization mapping in Pb-based ferroelectrics by combining annular dark-field and integrated differential phase contrast imaging.[13,14] Nevertheless, such experimental techniques have not been demonstrated in resolving the behavior of single isolated point defects, and are not yet practical to implement over a broad range of compositions and conditions. This motivates the development of reliable computational approaches to predict and quantify the factors controlling defect polarizability more directly and more efficiently than possible with present experiments.

Computationally, density functional theory (DFT) has known drawbacks in simulating defected semiconducting systems under an electric field accurately. For defects with an in-gap state in semiconducting systems, pure DFT gives rise to an incorrect metallic solution[15,16] such that polarization calculations with the Berry phase approach[17,18] are inapplicable. DFT augmented with Hubbard *U* terms (DFT + *U*) is necessary to ensure localized defect states in a semiconducting system, but this approach significantly underestimates the materials' polarization response under an electric field.[5,19,20] Although hybrid functionals can address these challenges, such a method is currently not implemented with the Berry phase approach to perform ion relaxation under electric field. For the Quantum Espresso package 6.4.1[21,22] used in this study, the iteration processes of these two

Y.-T. Chi, K. J. Van Vliet, M. Youssef, B. Yildiz
Department of Materials Science & Engineering
Massachusetts Institute of Technology
Cambridge, MA 02139, USA
E-mail: krystyn@mit.edu; mostafa.youssef@aucegypt.edu;
byildiz@mit.edu
M. Youssef
Department of Mechanical Engineering
The American University in Cairo
AUC Avenue, P.O. Box 74, New Cairo 11835, Egypt
B. Yildiz
Department of Nuclear Science & Engineering
Massachusetts Institute of Technology
Cambridge, MA 02139, USA

approaches would interfere with each other, resulting in questionable results for a self-consistent single-shot calculation, and fail to converge for ionic relaxation. Therefore, we use a "local Hubbard U" method to circumvent these challenges in this work.

Here, we deconvolute the role of two factors that we hypothesize to affect the polarizability of a point defect in complex oxides: lattice volume and reducibility of ions surrounding the point defect. Specifically, we assessed the polarizability of the neutral oxygen vacancy, characterized by two electrons trapped in the vacant site (color center, singlet state) in an ABO_3 cubic perovskite oxide under electric field (see Section S1, Supporting Information, for defect magnetic configuration comparison). First, we resolved the defect dipole moment as a function of lattice volume, tuned by elastic strain in $SrTiO_3$ or by changing the A-site cation species (A = Sr or Ba). $BaTiO_3$ has a larger A-site cation and lattice volume compared to $SrTiO_3$, otherwise maintaining the same transition metal and reduction–oxidation (redox) chemistry. Second, we resolved the role of reducibility of the B-site transition metal cation surrounding the defect by varying the B-site cation in $BaBO_3$ (B = Ti, Zr, or Hf) while keeping the same crystallographic symmetry and the same lattice volume (when needed) by applying hydrostatic strain. It is worth noting that the structural ground states for $SrTiO_3$, $BaZrO_3$, and $BzHfO_3$ are already in the cubic phase under room temperature,[23,24] and selecting cubic $BaTiO_3$ (high temperature phase) is necessary to facilitate a consistent comparison under the same crystallographic symmetry. The coupling of the defect polarization and the ferroelectric $BaTiO_3$ phase is beyond the scope of the current study, but could be of interest in further work.

Let us consider the rationale for why these two factors could each influence point defect polarizability. Volumetric changes in an ABO_3 crystal can be introduced via applied mechanical strain, or by composition (i.e., varying the A-site cation at zero strain). Increasing free volume around a point defect alters the potential energy landscape around the defect, reducing the electronic interaction of that defect with its surroundings.[25,26] This means that the increased free volume around a neutral oxygen vacancy studied here reduces the constraints on the electron density occupying that volume, thereby making it easier for the trapped electrons to polarize under an electric field. We have also shown previously that lattice volume increase due to cation size among several simple binary oxides affects the polarizability of oxygen vacancies.[5]

Reducibility of transition metal ions surrounding the neutral oxygen vacancy can also play an important role in affecting the polarizability of the trapped electrons at the vacant site. By reducibility, we mean the ease of reduction of the cation by gaining a localized electron and formally changing its oxidation state. This is related to the energy levels of the electron defect state projected on that cation. It is possible to calculate these reduction–oxidation (redox) levels for each compound and defect type. However, in the spirit of establishing a simpler descriptor, we adopt electronegativity of the neutral transition metal to represent the reducibility of its charged cation. For metal elements of high electronegativity, we expect the corresponding ions should attract electrons more easily than those of metals with lower electronegativity. We can justify this hypothesis also by observing that the previously reported polarization of $BiMO_3$ (M = Al, Ga, Fe)[27–29] correlates positively with the electronegativity of the B-site cation. The po-

larization of the lone-pair electrons on bismuth share some similarities with the polarization of the two trapped electrons in the oxygen vacancy treated in this work; they are both associated with local electronic states, the spatial distribution of which depends on the species of nearby ions.

2. Results

2.1. Modeling Defect Polarization under Electric Field Using a Local Hubbard U Method

To address the challenges in studying the polarization of defective semiconducting oxides using DFT, we have adopted an approach based on the previously reported self-consistent, site-dependent DFT + U method.[30,31] This approach applies different Hubbard U magnitudes on different lattice sites in a defected system, especially for the sites closest to the defect. In our work, to minimize the potentially detrimental effect of Hubbard U on the polarization properties, we applied the Hubbard U correction only on the two Ti ions adjacent to the oxygen vacancy site to ensure charge localization, and we termed this approach the "local Hubbard U". Choosing a very low magnitude of U (1 or 2 eV) would not achieve enough electron localization on the defect site, as confirmed by hybrid functionals.[32,33] A very high magnitude (>5 eV), on the other hand, would result in unphysical over localization. We tested U = 3, 4, and 5 eV and chose to implement U = 5 eV in our following study, since this magnitude resulted in consistent results between a 3 × 3 × 3 supercell and a 2 × 2 × 2 supercell. However, all magnitudes of U considered led to similar trends albeit with different magnitudes. Full methodology details are provided in Sections S1 and S 2, Supporting Information, while the framework and definitions are summarized here in **Figure 1**. As shown in Figure 1a, we constructed a 2 × 2 × 2 $SrTiO_3$ supercell with one neutral oxygen vacancy (V_O^x with Kroger–Vink notation). We applied a Hubbard U correction[34] of 5.0 eV only to the d-states of the two Ti ions neighboring the oxygen vacancy, depicted as dark blue spheres. Figure 1b shows the density of states, illustrating that the local Hubbard U is sufficient to localize the two electrons in the defect site leading to a correct in-gap electronic state under the electric field. At the same time, this approach together with the modern theory of polarization[18,35] yields a static permittivity of the overall defective crystal close to the experimental value.[36,37] Comparisons of static permittivity and polarization results arising from the standard Hubbard U and the local Hubbard U methods are shown in Figures 1c and 1d, respectively. The non-linear polarization under low electric field predicted with the local Hubbard U better reflects the high static permittivity for $SrTiO_3$ under low field as shown in Figure 1c), where the difference was attributed to slightly different lattice constants obtained by DFT and experiment. Using the local Hubbard method with the experimentally determined lattice constant of $SrTiO_3$, our predicted static permittivity matches very well with the experimental static permittivity values[37] under all fields (see Section S1, Supporting Information). Note that the bandgap of $SrTiO_3$ obtained with the local Hubbard U method under zero field (2.54 eV) underestimates the experimental value (3.2 eV[38]), which we attributed to the intentional lack of a global Hubbard U correction on all the other Ti and O ions in our simulation. Despite the inaccurate bandgap,
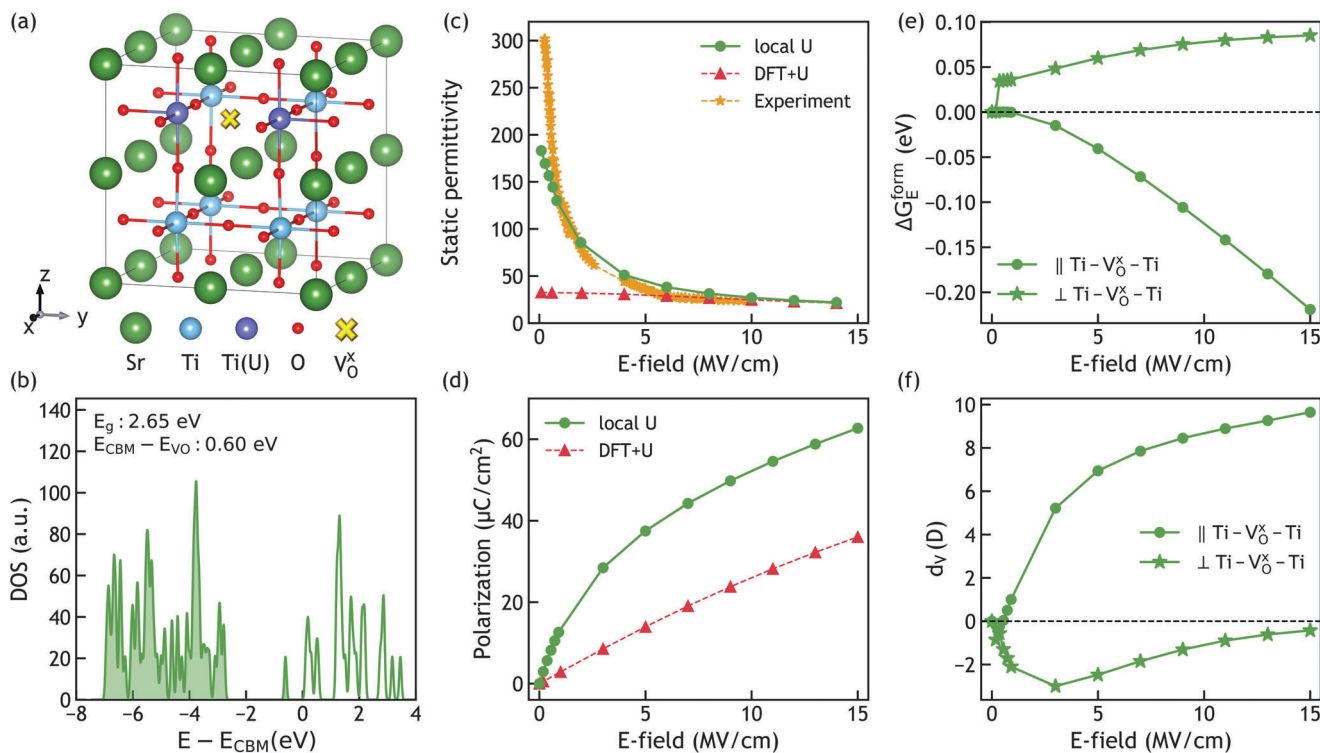
**ADVANCED
SCIENCE NEWS**

www.advancedsciencenews.com

**ADVANCED
SCIENCE**
Open Access

www.advancedscience.com

Figure 1. Density of states, dielectric properties and defect formation energy predicted for neutral oxygen vacancy V_O^x in SrTiO$_3$, using density functional theory with local Hubbard U. a) A $2 \times 2 \times 2$ SrTiO$_3$ super cell with V_O^x. Green, light blue, and red spheres represent Sr, Ti, and O ions, respectively. Dark blue spheres indicate the two Ti ions with local Hubbard U, adjacent to the trapped electrons in the oxygen vacancy site represented by a yellow cross. All crystals in this work were visualized by VESTA.[41] b) Density of states for defected SrTiO$_3$ under 3 MV cm^{-1} with shaded area representing occupied states. E_g and E_{CBM} are the band gap and the minimum energy of conduction band, respectively. E_{CBM} is set to be zero. Static dielectric permittivity (c) and polarization (d) of defected SrTiO$_3$ with respect to applied electric field parallel to the Ti^{4+} − V_O^x − Ti^{4+} chain direction, from 0 to 15 MV cm^{-1}, using the local Hubbard U method (green circles), standard DFT + U method (red triangles), and the experimental values (orange stars). The non-linear polarization predicted by local Hubbard U better reflects the high static permittivity of SrTiO$_3$ under low field. Comparison of relative electric Gibbs free energy of formation of V_O^x (e), and the vacancy dipole d_V in units of Debye (f) with respect to applied field parallel to (circles) and perpendicular to (stars) the Ti^{4+} − V_O^x − Ti^{4+} chain.

we believe our method provides the best compromise between defect and dielectric properties in semiconducting oxides with the current simulation package capabilities.

Having established a method to study defected SrTiO$_3$ under electric field, we recall the definition of electric Gibbs free energy of formation G_E^{form} for a neutral oxygen vacancy[5] V_O^x:

$$G_E^{form} = \left(U^{def} - U^{perf} + \mu_O \right) - V\vec{E} \cdot \left(\vec{P}^{def} - \vec{P}^{perf} \right) \quad (1)$$

where U and P are the internal energy and polarization of the defect-free (perf) or defected (def) SrTiO$_3$ under electric field, respectively; μ_O is the chemical potential of oxygen; V is the volume of the supercell; and $\vec{E}$ is the electric field. The net dipole moment in the system arising from the introduction of V_o^x into the system d_V is given through the last term in Equation (1):

$$d_V = V \cdot \left(\vec{P}^{def} - \vec{P}^{perf} \right) \quad (2)$$

We will call this quantity the oxygen vacancy dipole moment, although with such definition this is not the dipole moment locally calculated at the vacant site. Instead, it is the difference between the dipole moments of the defected and perfect crystals due to the creation of one oxygen vacancy. By performing site-decomposed dipole moment analysis using Wannier functions,[39,40] we found that the two electrons at the oxygen vacant site in SrTiO$_3$ contribute largely to d_V (see Section S5, Supporting Information), consistent with our previous work on binary oxides.[5]

Figure 1e shows ΔG_E^{form} as a function of electric field, and it is defined as the difference in V_O^x formation energy between finite and zero field conditions. When the electric field was applied parallel to the Ti^{4+} − V_O^x − Ti^{4+} chain, ΔG_E^{form} decreased with increasing field magnitude. Note that each oxide ion is twofold coordinated by Ti in SrTiO$_3$. In contrast, when the field was applied perpendicular to the Ti^{4+} − V_O^x − Ti^{4+} chain, ΔG_E^{form} increased with increasing field. As such we conclude that the electric field breaks the symmetry of the crystal and creates two populations of oxygen sites; those with Ti^{4+} − V_O^x − Ti^{4+} chains aligned parallel to the field, and those with chains perpendicular to the field. At zero field, both populations are equally likely to host a vacancy. Under
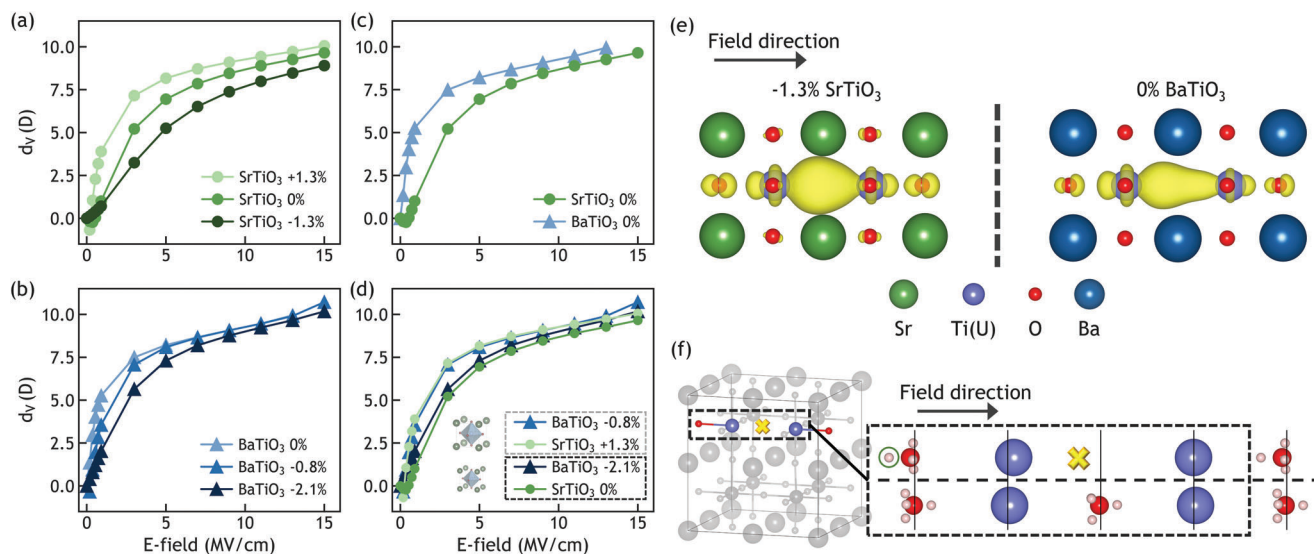
**ADVANCED
SCIENCE NEWS**

www.advancedsciencenews.com

**ADVANCED
SCIENCE**
Open Access

www.advancedscience.com

Figure 2. Oxygen vacancy dipole moment d_V in SrTiO$_3$ and BaTiO$_3$ with field applied parallel to the Ti^{4+} − V_O^x − Ti^{4+} chain. The d_V for hydrostatically strained a) SrTiO$_3$ and b) BaTiO$_3$. Comparison of d_V for c) unstrained and d) strained SrTiO$_3$ and BaTiO$_3$. Legend in (d) groups the SrTiO$_3$ and BaTiO$_3$ configurations that have the same lattice volume due to applied hydrostatic strains, where + indicates applied hydrostatic tension, and − indicates hydrostatic compression. e) Charge density of two trapped electrons in the vacant site of −1.3% compressed SrTiO$_3$ (left) and unstrained BaTiO$_3$ (right) under 3 MV cm^{-1}. Isosurfaces are taken at 3% of the maximum value, with the V_o^x defect energy levels being 0.49 and 0.35 eV below conduction band minimum for SrTiO$_3$ and BaTiO$_3$, respectively. f) The O − Ti^{4+} − V_O^x − Ti^{4+} chain in SrTiO$_3$, with enlarged view showing the displacement of the sites in the chain (top), comparing with the corresponding sites in defect-free cell (bottom) at 3 MV cm^{-1}. Solid vertical lines represent the origins of each site under zero field, the yellow cross and light pink spheres represent the Wannier centers of the electron pairs of the vacancy trapped electrons and oxide ions, respectively. The Wannier centers on Ti ions are not shown.

a finite field, the chain parallel to the field (1/3 of the total oxygen population) is more likely to host a vacancy. ΔG_E^{form} is determined mainly by the d_V defined above, and to a much lesser extent by the change in the internal energy (see first term in Equation (1), with details in Section S2, Supporting Information). Figure 1f shows the effect of the electric field direction on d_V in SrTiO$_3$, exhibiting a sign dependence of d_V on the field direction with respect to the Ti^{4+} − V_O^x − Ti^{4+} chain. With field applied parallel to <100> in cubic SrTiO$_3$, the trapped electrons would either be polarized toward one of the neighboring Ti ions (field parallel to the Ti^{4+} − V_O^x − Ti^{4+}, which is the case for 1/3 of the oxygen sites); or toward the space between the nearest Sr ions (field perpendicular to the Ti^{4+} − V_O^x − Ti^{4+}, which is the case for 2/3 of the oxygen sites). Positive d_V and decreasing ΔG_E^{form} are consistent with the favored polarization direction being parallel to the Ti^{4+} − V_O^x − Ti^{4+} chain. To focus the discussion on the dominant vacancy population, the results below are concerned primarily with the electric field applied parallel to the Ti^{4+} − V_O^x − Ti^{4+} chain.

2.2. Lattice Volume Effect on Oxygen Vacancy Dipole Moment, d_V

Having adapted a reliable computational approach to accurately predict the electronic and ionic structure, static permittivity, and polarization in a semiconducting perovskite, we sought to assess the role of the two hypothesized factors: lattice space available for the defect, and electronegativity of the cations closest to the defect site. To test the former, we tuned the lattice volume by lattice strain and A-site cation size. It is worth noting that all the mate-

rials studied here did not undergo any phase change/distortion under the strains and electric fields considered in this study.

In our simulations, we have applied hydrostatic strains to SrTiO$_3$ to isolate the effect of lattice volume on polarizability without altering crystal symmetry. **Figure 2**a shows that the d_V for SrTiO$_3$ increased with increasing tensile strain (+1.3% hydrostatic expansion of lattice parameter), relative to unstrained SrTiO$_3$ under the same applied field. Hydrostatically compressed (−1.3%) SrTiO$_3$ exhibited the lowest d_V, except under the lowest applied field (<0.5 MV cm^{-1}). To further validate the role of lattice volume in determining d_V, we altered the A-site cation from Sr to Ba to increase the lattice volume. At zero strain, BaTiO$_3$ exhibited higher d_V than SrTiO$_3$, as shown in Figure 2b,c; this is consistent with the expected lattice volume effect. Nevertheless, Ba ions not only result in a larger lattice volume, but alter the A-site composition. To confirm that the difference between these two compounds arises predominantly from the lattice volume, we strained BaTiO$_3$ by −2.1% to match the lattice parameter of unstrained SrTiO$_3$, and by −0.8% to match the lattice parameter of +1.3% strained SrTiO$_3$. The magnitude of d_V for SrTiO$_3$ and BaTiO$_3$ were the same in both of these cases with identical lattice volumes, as shown in Figure 2d. The slight differences between unstrained SrTiO$_3$ and compressed BaTiO$_3$ of the same lattice volume are attributable to the large compressive strain on BaTiO$_3$ (Section S5, Supporting Information). These results indicate that the d_V is mainly sensitive to the lattice volume and the effective volume of the oxygen vacancy site when the alkaline earth cations on the A-site have very similar chemistry (Sr, Ba). Figure 2e also shows the charge density of the two trapped electrons in the vacant site for the smallest and the largest lattice

parameters involved in this comparison—the compressed (−1.3%) $SrTiO_3$ and the unstrained $BaTiO_3$ under 3 MV cm^{-1}. The charge distribution in the unstrained $BaTiO_3$ is clearly more polarized owing to the larger vacant site space, resulting in higher polarization under the same field strength, compared with that in the compressed (−1.3%) $SrTiO_3$.

2.3. Site Decomposed Polarization at and around the Oxygen Vacancy

To further understand the underlying physics of d_V, we utilized Wannier calculations[39,40] and decomposed d_V into the field-induced dipole moment of each site in the system. We found that not only the trapped electrons but the whole $O − Ti^{4+} − V_O^x − Ti^{4+}$ chain promotes d_V via both ionic and electronic displacements, as illustrated in Figure 2f. First, as the Ti cations and trapped electrons are of opposite charge, they were polarized in opposite directions by the electric field: one of the Ti ions in the $Ti^{4+} − V_O^x − Ti^{4+}$ chain approached the trapped electrons with increasing field, whereas the other ion receded further away. Second, and most importantly, the approaching Ti ion and the Wannier center of the trapped electrons both showed larger displacements than the corresponding sites in the defect-free cell (Ti and O ion, respectively), contributing strongly and positively to d_V, as shown in Figure 2f. We believe this is a result of the strong attraction between the Ti ion and the two electrons without the confinement of the oxygen atom potential, as well as the ease of reducing the Ti^{4+} to Ti^{3+} (high electronegativity of Ti). Third, the O ion in the $O − Ti^{4+} − V_O^x − Ti^{4+}$ chain also promoted d_V owing to the circled Wannier center with large displacement under electric field shown in Figure 2f. Last, the receding Ti ion only showed slightly larger displacement in the defected cell than the corresponding site in the defect-free cell. We found that up to 75% of d_V is contributed by the $O − Ti^{4+} − V_O^x − Ti^{4+}$ defect cluster, whereas other sites further away from the vacant site had polarization comparable to the corresponding sites in the perfect cell (See Section S5, Supporting Information, for detailed site-decomposed polarization analyses[42]).

2.4. B site Cation Reducibility Effect on Oxygen Vacancy Dipole Moment, d_V

Next, to test the hypothesis that the reducibility of the cation affects the polarizability of the trapped electrons nearby, we have used different transition metals on the B-site of the perovskite, in particular $BaTiO_3$, $BaZrO_3$, and $BaHfO_3$. As we noted above, we use electronegativity of a metal as a simpler measure of the reducibility of the metal cation. Prior work has shown that Ti ions in $SrTiO_3$ and TiO_2 can easily form polaronic defects[43,44] ($Ti^{4+} + e^− → Ti^{3+}$), whereas Zr and Hf ions in ZrO_2 and HfO_2, respectively, would be energetically disfavored to form polaronic defects.[45–48] Not all of these ABO_3 compounds $(Sr,Ba)(Ti,Hf,Zr)O_3$ are stable in the cubic phase[23,49,50] and we observed significant structural distortion in $SrZrO_3$ and $SrHfO_3$ simply by introducing the oxygen vacancy. Therefore, we focused on the Ba-based cubic perovskites with different B-site cations of 4+ valence: $BaBO_3$ (B = Ti, Zr, Hf), with the electronegativity of Ti, Zr, and Hf being

1.54, 1.33, and 1.30,[51] respectively. To facilitate comparison of d_V as a function of electronegativity, we maintained the same lattice constant by imposing different hydrostatic strains to each of the three perovskites. We applied electric field parallel to the $B^{4+} − V_O^x − B^{4+}$ (B = Ti, Zr, Hf) chain and strained $BaZrO_3$ and $BaHfO_3$ by −5% and −4.3%, respectively, to match the lattice constant of unstrained $BaTiO_3$. As shown in **Figure 3**a, hydrostatically compressed $BaZrO_3$ (−5%) and $BaHfO_3$ (−4.3%) exhibited similar d_V, and these d_V were much lower than that of unstrained $BaTiO_3$. This result confirms that d_V increases with the electronegativity of the B-site cation neighboring the trapped electrons at the oxygen vacancy site.

However, the simulated compressive strains were impractically large for $BaZrO_3$ and $BaHfO_3$ (−5% and −4.3%, respectively). To avoid potential artifacts introduced by such large strains, we have also applied smaller strains on $BaHfO_3$ (+0.8%) and $BaZrO_3$ (−0.7%) to match the lattice constants of unstrained $BaZrO_3$ and $BaHfO_3$, respectively. First, as shown in Figure 3b, although all four d_V responses were similar in overall trend and magnitude, none were identical even when $BaZrO_3$ and $BaHfO_3$ had matching lattice volumes. Furthermore, all d_V were negative in both $BaZrO_3$ and $BaHfO_3$ under zero or small strain when the field was applied parallel to the $B^{4+} − V_O^x − B^{4+}$ (B = Zr, Hf) chain, indicating that this polarization direction is unfavorable in defective $BaZrO_3$ and $BaHfO_3$, in contrast to $SrTiO_3$ and $BaTiO_3$. We found a correlation between the favored polarization direction (positive d_V) and the charge density distribution of the trapped electrons in $BaBO_3$ (B = Ti, Zr, Hf) under zero field and strain. As shown in Figure 3c, the electron charge density is elongated toward to the two neighboring Ti ions in unstrained $BaTiO_3$ at zero field. We believe that such a highly anisotropic charge distribution indicates the favored and unfavored polarization directions, which were parallel and perpendicular to the $Ti^{4+} − V_O^x − Ti^{4+}$ chain, respectively. By contrast, the charge density distribution of V_O^x in $BaZrO_3$ and $BaHfO_3$ is more isotropic, and showed slight repulsion from the neighboring Zr or Hf ions. The resulting slightly elongated charge distribution perpendicular to the $B^{4+} − V_O^x − B^{4+}$ (B = Zr, Hf) chain suggested that the trapped electrons can more favorably polarize perpendicular to the $B^{4+} − V_O^x − B^{4+}$ (B = Zr, Hf) chain, albeit with a weaker polarization.

2.5. Favored Polarization Direction

Figure 3d,e shows the d_V for unstrained $SrTiO_3$, $BaTiO_3$, $BaZrO_3$, and $BaHfO_3$ with field applied either parallel (circles) or perpendicular (stars) to the $B^{4+} − V_O^x − B^{4+}$ (B = Ti, Zr, Hf) chains. Here, d_V was positive in $(Sr, Ba)TiO_3$ when electric field was applied parallel to the $Ti^{4+} − V_O^x − Ti^{4+}$ chain (the favorable polarization direction). In contrast, $BaZrO_3$ and $BaHfO_3$ exhibited positive d_V when the field was perpendicular to the $B^{4+} − V_O^x − B^{4+}$ (B = Zr, Hf) chain and negative d_V when the field was parallel to this chain. This confirms our above proposed correlation between the charge distribution shape at zero-field and the favored polarization direction (sign of d_V). Furthermore, Figure 3d,e also show that increased lattice volume ($V_{SrTiO_3} < V_{BaTiO_3}$, $V_{BaHfO_3} < V_{BaZrO_3}$) correlated with increasingly positive d_V when field was applied along the favored polarization direction, and more negative d_V
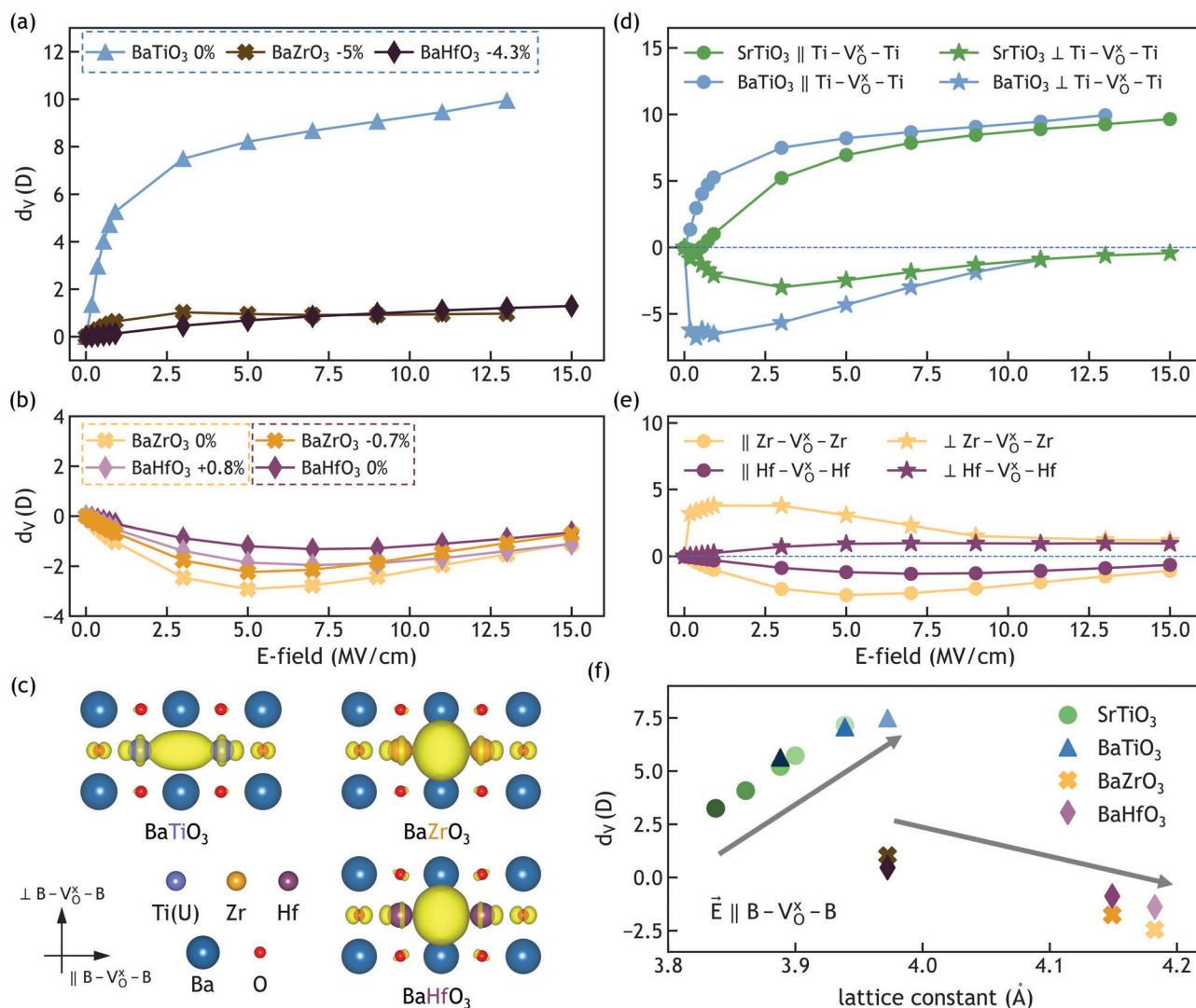
**ADVANCED
SCIENCE NEWS**

www.advancedsciencenews.com

**ADVANCED
SCIENCE**
Open Access

www.advancedscience.com

Figure 3. Oxygen vacancy dipole moment d_V and charge density distribution of the trapped electrons in Ba(Ti, Zr, Hf)O$_3$. The d_V of BaTiO$_3$, BaZrO$_3$, and BaHfO$_3$ with field applied parallel to $B^{4+} - V_O^x - B^{4+}$ (B = Ti, Zr, Hf), with the latter two compounds a) compressively strained to match the lattice constant of unstrained BaTiO$_3$, and b) strained either in tension (BaHfO$_3$) or compression (BaZrO$_3$) to match the lattice constant of each other. The dotted boxes group the Ba-based perovskites with the same lattice volume. c) Charge density of the two trapped electrons in BaTiO$_3$, BaZrO$_3$, and BaHfO$_3$ under zero strain and zero field strength, showing distinct isosurface shapes with different B-site cations. Isosurfaces are taken as 3% of the maximum value for BaTiO$_3$, and 10% for BaZrO$_3$ and BaHfO$_3$ with defect energy levels being 0.35, 0.68, 1.15 eV below conduction band minimum for BaTiO$_3$, BaZrO$_3$, and BaHfO$_3$, respectively. d_V for unstrained d) SrTiO$_3$ (green), BaTiO$_3$ (blue), and e) BaZrO$_3$ (orange), BaHfO$_3$ (purple) with field applied parallel (circles) or perpendicular (stars) to the $B^{4+} - V_O^x - B^{4+}$ chain. f) d_V for all compounds under different strain states and an electric field of 3 MV cm^{-1} parallel to the $B^{4+} - V_O^x - B^{4+}$ chain as a function of lattice constant of the compound.

when the field was applied perpendicular to the favored polarization direction of the material. In Figure 3f, we summarize d_V with respect to lattice constant under an applied field of 3 MV cm^{-1} (obtained for the four different perovskite compositions with different strains); field was applied parallel to the $B^{4+} - V_O^x - B^{4+}$ (B = Ti, Zr, Hf) chains. Because this is the favored polarization direction in (Sr, Ba)TiO$_3$, d_V increased positively and also increased linearly with increasing lattice constant. In contrast, d_V became more negative with increasing lattice volume in Ba(Zr, Hf)O$_3$ for which the favored polarization is perpendicular to the $B^{4+} - V_O^x - B^{4+}$ chain.

The oxygen vacancy dipole moment d_V depends chiefly on the dipole moment of the defect cluster ($O - B^{4+} - V_O^x - B^{4+}$, B = Ti, Zr, Hf) in these ABO_3 perovskite compounds. The dipole moment of the main segment ($B^{4+} - V_O^x - B^{4+}$) of this defect cluster is determined by the localization of the trapped electrons at V_O^x and their interaction with the neighboring B-site cation under electric field, both correlated closely with the electronegativity of the B-site cation.

Figure 4 illustrates magnitudes and trends for the dipole moment of the defect cluster and oxygen vacancy, for several ABO_3 compositions each under varying magnitudes of relative com-
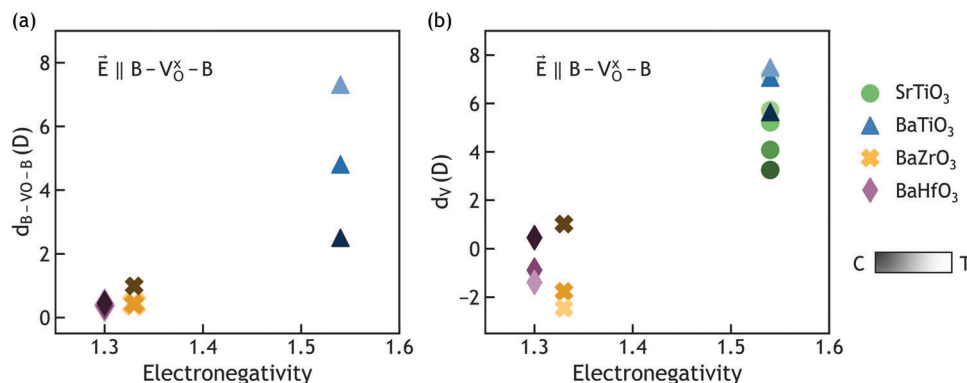
Figure 4. Defect cluster dipole and oxygen vacancy dipole moment with electric field applied parallel to $B^{4+} - V_O^x - B^{4+}$. a) The defect cluster $B^{4+} - V_O^x - B^{4+}$ dipole moment, d_{B-VO-B}, under 1 MV cm^{-1} as a function of electronegativity of the B-site element. b) The net dipole moment introduced by oxygen vacancy, d_V, for all compounds under different strain states and an electric field of 3 MV cm^{-1} as a function of electronegativity of the B-site element. Multiple points for each compound represent differently strained lattice parameter, where transitions from darker to lighter shades of a given colored symbol indicate strain variation from relative compression (C) to tension (T).

pression or tension. It is worth noting that d_{B-VO-B} is a local dipole calculated in the defected crystal, whereas d_V is a difference in the overall dipole moments of both defected and perfect crystals. In Figure 4a, we show the local dipole moment of the $B^{4+} - V_O^x - B^{4+}$ chain (B = Ti, Zr, Hf), d_{B-VO-B}, with a strong positive correlation to the electronegativity of the B-site cation. The effect of lattice strain also highly depends on the electronegativity of the B-site cation, where the strain alters d_{B-VO-B} significantly in BaTiO$_3$, has a moderate effect on BaZrO$_3$, and has minimal effect on BaHfO$_3$. Although Zr and Hf are physically and chemically similar, they still have slightly different electronegativities[51] and reducibilities,[52] resulting in different d_{B-VO-B} and d_V under the same lattice volume, as well as in their responses to lattice strain. Finally, Figure 4b illustrates the same data as those in Figure 3f, now expressed as a function of B-site cation electronegativity in each compound (Ti, Zr, or Hf). Note the strong positive correlation between B-site cation electronegativity and d_V magnitude, consistent with our hypothesis that B-site cation reducibility modulates the core defect cluster dipole and the effective d_V under applied field.

In addition to the correlation we have identified between the defect polarization and the electronegativity of the B site cation, we also found that the electron effective mass at the conduction band minimum (CBM) correlated with defect polarization. We believe that the more reducible the B site cation (equivalent to higher electronegativity), the more easily it can "trap" the electron, which will lead to larger electron effective mass. Our band structure calculations on BaBO$_3$ (B = Ti, Zr, Hf) with the same lattice constant showed that both d_{B-VO-B} and d_V correlate positively with the electron effective masses at the conduction band minimum (CBM), similar to the correlation shown in Figure 4 (Section S6, Supporting Information).

3. Conclusions

In summary, a direct relationship exists between lattice volume and oxygen vacancy dipole moment in ABO_3 perovskites as a function the A-site cation size and/or lattice strain. This correlation affects the response of such materials to applied electric

field. Expanding the lattice volume increases the net dipole of the defective system d_V, if the field is applied in the direction of favorable polarization. In fact, with the same B-site cation, SrTiO$_3$ and BaTiO$_3$ strained to exhibit the same lattice constants and also exhibited identical d_V. The B-site cation species independently played an important role in affecting d_V, as illustrated for Ba(Ti, Zr, Hf)O$_3$ in which the B site cation electronegativity correlated positively with d_V and the local dipole moment of the defect cluster d_{B-VO-B}. The electronegativities of the B site cations thus showed great influence on defect formation energies under electric field. The preferred polarization direction of defects also varied with the effective electronegativity of the B-site cation, which indicated different defect ordering, parallel or perpendicular, with respect to the field. The local Hubbard U approach presented in this work provides a cost-efficient and presently accessible method to study defected semiconducting perovskite oxides under electric field, while having some limitations regarding the electronic structure of the material. We believe our framework provides a general method for the analysis of defected semiconducting oxides under electric field. Our findings regarding the stability and properties of defects that are polarized under strong electric fields can enable development of more accurate physical models of predicting the behavior of thin-film redox based memristors.[1,2]

4. Methods

In this study, the authors conducted all DFT and Berry phase simulations[17,18] with the Quantum Espresso package version 6.4.1.[21,22] The plane-wave kinetic energy cutoff was set to 100 Ry and charge density cutoff to 400 Ry. Optimized norm-conserving Vanderbilt pseudopotentials, NCSR (ONCVPSP v0.4), from PseudoDojo[53,54] with Perdew–Burke–Ernzerhof exchange-correlation functional for solids (PBEsol)[55] are used in this study. Lattice constants for ABO_3 (A = Ca, Sr and Ba; B = Ti, Zr and Hf) were obtained using 21 different volumes, fitted with the 3rd order Birch–Murnaghan equation of state.[56] Reciprocal space was sampled using 8 × 8 × 8 displaced Monkhorst-Pack k-point grid[57] with no smearing in all

calculations. All compounds were fitted under cubic symmetry constraint.

The authors conducted electric field simulations on $SrTiO_3$, $BaTiO_3$, $BaZrO_3$, and $BaHfO_3$ with Berry phase approach (lelfield = .true.) and modern theory of polarization.[17,58] Local Hubbard U correction was applied on Ti but not on Zr nor Hf, since wide bandgap materials such as $BaZrO_3$ and $BaHfO_3$ do not require such a correction to obtain a correct in-gap defect state under electric field. Hubbard U was applied using the DFT + U simplified version by Cococcioni and de Gironcoli,[34] which corresponded to "lda_plus_u_kind = 0" in Quantum ESPRESSO. The authors used $2 \times 2 \times 2$ supercell on both perfect and defective systems, with reciprocal space sampled using $2 \times 2 \times 2$ Monkhorst-Pack k-point grid,[57] displaced by (0.5 0.5 0.5).

For field applied either parallel or perpendicular to the $B^{4+} - V_O^x - B^{4+}$ (B = Ti, Zr, Hf) chain, the authors relaxed the system fully within two field strength regimes: low field {0, 0.00005, 0.00010, 0.00015, 0.00020, 0.00025} in Ry atomic units, and high field {3, 5, 7, 9, 11, 13, 15} MV cm^{-1}. Note that 0.00005 Ry is $\approx$0.2 MV cm^{-1}. Under every field, electronic and ionic structures were allowed to fully relax, while the shape and lattice constant were constrained. They set the convergence condition for electronic structure relaxation to be 10^{-9} Ry, and ionic relaxation stopping criteria to be 4×10^{-6} Ry for total energy and 4×10^{-5} Ry/bohr for forces. Spin was not considered in their calculations. They adopted their previous method[5] and applied small Gaussian smearing (0.004 Ry) to speed their calculation with no fractional occupations

Supporting Information

Supporting Information is available from the Wiley Online Library or from the author.

Acknowledgements

Conflict of Interest

The authors declare no conflict of interest.

Data Availability Statement

The data that support the findings of this study are available from the corresponding author upon reasonable request.

Keywords

[1] R. Waser, R. Dittmann, G. Staikov, K. Szot, *Adv. Mater.* **2009**, *21*, 2632.

[2] M. Kubicek, R. Schmitt, F. Messerschmitt, J. L. M. Rupp, *ACS Nano* **2015**, *9*, 10737.

[3] K. Maas, E. Villepreux, D. Cooper, E. Salas-Colera, J. Rubio-Zuazo, G. R. Castro, O. Renault, C. Jimenez, H. Roussel, X. Mescot, Q. Rafhay, M. Boudard, M. Burriel, *Adv. Funct. Mater.* **2020**, *30*, 1909942.

[4] P. Sriboriboon, H. Qiao, S. Kang, C. Sun, Y. Kim, *Adv. Funct. Mater.* https://doi.org/10.1002/adfm.202103145.

[5] M. Youssef, K. J. Van Vliet, B. Yildiz, *Phys. Rev. Lett.* **2017**, *119*, 126002.

[6] N. Salles, L. Martin-Samos, S. de Gironcoli, L. Giacomazzi, M. Valant, A. Hemeryck, P. Blaise, B. Sklenard, N. Richard, *Nat. Commun.* **2020**, *11*, 3330.

[7] W. Hu, Y. Liu, R. L. Withers, T. J. Frankcombe, L. Norén, A. Snashall, M. Kitchin, P. Smith, B. Gong, H. Chen, J. Schiemer, F. Brink, J. Wong-Leung, *Nat. Mater.* **2013**, *12*, 821.

[8] Y. Yang, R. Huang, *Nat. Electron.* **2018**, *1*, 274.

[9] W. Lü, C. Li, L. Zheng, J. Xiao, W. Lin, Q. Li, X. R. Wang, Z. Huang, S. Zeng, K. Han, W. Zhou, K. Zeng, J. Chen, Ariando, W. C., T. Venkatesan, *Adv. Mater.* **2017**, *29*, 1606165.

[10] Z. Wang, H. Wu, G. W. Burr, C. S. Hwang, K. L. Wang, Q. Xia, J. J. Yang, *Nat. Rev. Mater.* **2020**, *5*, 173.

[11] W. Gao, C. Addiego, H. Wang, X. Yan, Y. Hou, D. Ji, C. Heikes, Y. Zhang, L. Li, H. Huyan, T. Blum, T. Aoki, Y. Nie, D. G. Schlom, R. Wu, X. Pan, *Nature* **2019**, *575*, 480.

[12] A. Kumar, J. N. Baker, P. C. Bowes, M. J. Cabral, S. Zhang, E. C. Dickey, D. L. Irving, J. M. LeBeau, *Nat. Mater.* **2021**, *20*, 62.

[13] I. Lazić, E. G. T. Bosch, S. Lazar, *Ultramicroscopy* **2016**, *160*, 265.

[14] N. Shibata, S. D. Findlay, H. Kohno, H. Sawada, Y. Kondo, Y. Ikuhara, *Nat. Phys.* **2012**, *8*, 611.

[15] M. Li, J. Li, L.-Q. Chen, B.-L. Gu, W. Duan, *Phys. Rev. B* **2015**, *92*, 115435.

[16] K. Klyukin, V. Alexandrov, *Phys. Rev. B* **2017**, *95*, 035301.

[17] I. Souza, J. Íñiguez, D. Vanderbilt, *Phys. Rev. Lett.* **2002**, *89*, 117602.

[18] N. A. Spaldin, *J. Solid State Chem.* **2012**, *195*, 2.

[19] L. L. Tao, J. Wang, *J. Appl. Phys.* **2016**, *119*, 224104.

[20] X. Liu, J. D. Burton, E. Y. Tsymbal, *Phys. Rev. Lett.* **2016**, *116*, 197602.

[21] P. Giannozzi, O. Andreussi, O. Brumme, O. Bunau, M. B. Nardelli, M. Calandra, R. Car, C. Cavazzoni, D. Ceresoli, M. Cococcioni, N. Colonna, I. Carnimeo, A. D. Corso, S. de Gironcoli, P. Delugas, R. A. DiStasio, Jr, A. Ferretti, A. Floris, G. Fratesi, G. Fugallo, R. Gebauer, U. Gerstmann, F. Giustino, T. Gorni, J. Jia, M. Kawamura, H.-Y. Ko, A. Kokalj, E. Küçükbenli, M. Lazzeri, et al., *J. Phys.: Condens. Matter* **2017**, *29*, 465901.

[22] P. Giannozzi, S. Baroni, N. Bonini, M. Calandra, R. Car, C. Cavazzoni, D. Ceresoli, G. L. Chiarotti, M. Cococcioni, I. Dabo, A. D. Corso, S. de Gironcoli, S. Fabris, G. Fratesi, R. Gebauer, U. Gerstmann, C. Gougoussis, A. Kokalj, M. Lazzeri, L. Martin-Samos, N. Marzari, F. Mauri, R. Mazzarello, S. Paolini, A. Pasquarello, L. Paulatto, C. Sbraccia, S. Scandolo, G. Sclauzero, A. P. Seitsonen, et al., *J. Phys.: Condens. Matter* **2009**, *21*, 395502.

[23] M. Noh, S. Choi, D. Lee, M. Cho, C. Jeon, Y. Lee, *New Phys.: Sae Mulli* **2013**, *63*, 939.

[24] L. Cao, E. Sozontov, J. Zegenhagen, *Phys. Status Solidi A* **2000**, *181*, 387.

[25] B. Yildiz, *MRS Bull.* **2014**, *39*, 147.

[26] A. Kushima, B. Yildiz, *J. Mater. Chem.* **2010**, *20*, 4809.

[27] P. Baettig, C. F. Schelle, R. LeSar, U. V. Waghmare, N. A. Spaldin, *Chem. Mater.* **2005**, *17*, 1376.

[28] J. Kaczkowski, *J. Mater. Sci.* **2016**, *51*, 9761.

[29] M. Fiebig, T. Lottermoser, D. Meier, M. Trassin, *Nat. Rev. Mater.* **2016**, *1*, 16046.

[30] C. Ricca, I. Timrov, M. Cococcioni, N. Marzari, U. Aschauer, *Phys. Rev. Res.* **2020**, *2*, 023313.

[31] C. Ricca, I. Timrov, M. Cococcioni, N. Marzari, U. Aschauer, *Phys. Rev. B* **2019**, *99*, 094102.

[32] Z. Hou, K. Terakura, *J. Phys. Soc. Jpn.* **2010**, *79*, 114704.

[33] A. Janotti, J. B. Varley, M. Choi, C. G. Van de Walle, *Phys. Rev. B* **2014**, *90*, 085202.

[34] M. Cococcioni, S. de Gironcoli, *Phys. Rev. B* **2005**, *71*, 035105.

[35] R. Resta, D. Vanderbilt, in *Physics of Ferroelectrics: A Modern Perspective*, Springer Berlin Heidelberg, Berlin, Heidelberg **2007**, p. 31.

[36] B. K. Choudhury, K. V. Rao, R. N. P. Choudhury, *J. Mater. Sci.* **1989**, *24*, 3469.

[37] R. A. van der Berg, P. W. M. Blom, J. F. M. Cillessen, R. M. Wolf, *Appl. Phys. Lett.* **1995**, *66*, 697.

[38] S. H. Wemple, *Phys. Rev. B* **1970**, *2*, 2679.

[39] N. Marzari, D. Vanderbilt, *Phys. Rev. B* **1997**, *56*, 12847.

[40] N. Marzari, A. A. Mostofi, J. R. Yates, I. Souza, D. Vanderbilt, *Rev. Mod. Phys.* **2012**, *84*, 1419.

[41] K. Momma, F. Izumi, *J. Appl. Crystallogr.* **2011**, *44*, 1272.

[42] G. Pizzi, V. Vitale, R. Arita, S. Blügel, F. Freimuth, G. Géranton, M. Gibertini, D. Gresch, C. Johnson, T. Koretsune, J. Ibañez-Azpiroz, H. Lee, J.-M. Lihm, D. Marchand, A. Marrazzo, Y. Mokrousov, J. I. Mustafa, Y. Nohara, Y. Nomura, L. Paulatto, S. Poncé, T. Ponweiser, J. Qiao, F. Thöle, S. S. Tsirkin, M. Wierzbowska, N. Marzari, D. Vanderbilt, I. Souza, A. A. Mostofi, et al., *J. Phys.: Condens. Matter* **2020**, *32*, 165902.

[43] A. Janotti, C. Franchini, J. B. Varley, G. Kresse, C. G. V. de Walle, *Phys. Status Solidi RRL* **2013**, *7*, 199.

[44] Y.-T. Chi, M. Youssef, L. Sun, K. J. Van Vliet, B. Yildiz, *Phys. Rev. Mater.* **2018**, *2*, 055801.

[45] K.-H. Xue, P. Blaise, L. R. C. Fonseca, Y. Nishi, *Phys. Rev. Lett.* **2013**, *110*, 065502.

[46] A. S. Foster, F. Lopez Gejo, A. L. Shluger, R. M. Nieminen, *Phys. Rev. B* **2002**, *65*, 174117.

[47] J. X. Zheng, G. Ceder, T. Maxisch, W. K. Chim, W. K. Choi, *Phys. Rev. B* **2007**, *75*, 104112.

[48] M. Youssef, B. Yildiz, *Phys. Rev. B* **2014**, *89*, 024105.

[49] M. Yashima, R. Ali, *Solid State Ionics* **2009**, *180*, 120.

[50] M. S. Paun, **2015**, https://doi.org/10.14279/depositonce-4796.

[51] J. E. Huheey, E. A. Keiter, R. L. Keiter, *Inorganic Chemistry : Principles of Structure and Reactivity*, HarperCollins College Publishers, New York, NY **1993**.

[52] D. Eder, R. Kramer, *Phys. Chem. Chem. Phys.* **2002**, *4*, 795.

[53] M. J. van Setten, M. Giantomassi, E. Bousquet, M. J. Verstraete, D. R. Hamann, X. Gonze, G.-M. Rignanese, *Comput. Phys. Commun.* **2018**, *226*, 39.

[54] D. R. Hamann, *Phys. Rev. B* **2013**, *88*, 085117.

[55] J. P. Perdew, A. Ruzsinszky, G. I. Csonka, O. A. Vydrov, G. E. Scuseria, L. A. Constantin, X. Zhou, K. Burke, *Phys. Rev. Lett.* **2008**, *100*, 136406.

[56] F. Birch, *Phys. Rev.* **1947**, *71*, 809.

[57] H. J. Monkhorst, J. D. Pack, *Phys. Rev. B* **1976**, *13*, 5188.

[58] P. Umari, A. Pasquarello, *Phys. Rev. Lett.* **2002**, *89*, 157602.

2104476 (9 of 9)